Photodissociation Study of 1,3-Dibromopropane at 234 nm via an Ion Velocity Imaging Technique

Ying Tang, Lei Ji, Rongshu Zhu, Zhengrong Wei, and Bing Zhang*

State Key Laboratory of Magnetic Resonance and Atomic and Molecular Physics, Wuhan Institute of Physics and Mathematics, Chinese Academy of Sciences, Wuhan 430071, PR China, and Graduate School of the Chinese Academy of Sciences, Beijing, PR China

Received: July 7, 2005; In Final Form: October 3, 2005

The photodissociation of 1,3-dibromopropane has been studied at 234 nm using a 2D photofragment ion velocity imaging technique coupled with a [2 + 1] resonance-enhanced multiphoton ionization scheme. The velocity distributions for the Br ($^2P_{1/2}$) (denoted Br*) and Br ($^2P_{3/2}$) (denoted Br) fragments are determined, and each can be fitted by a narrow single-peaked Gaussian curve, suggesting that bromine fragments are generated as a result of direct dissociation via repulsive potential energy surfaces. The recoil anisotropies were measured to be $\beta = 0.80$ for Br and 1.31 for Br*, and the product relative quantum yields at 234 nm is $\Phi_{234\ nm}(Br^*) = 0.21$.

1. Introduction

The ultraviolet photochemistry of halogen-containing organic compounds, especially the alkyl bromides, has attracted a great deal of attention in recent years because of their importance to stratosphere ozone destruction.[1−12] When excited in the first absorption continuum (A band), which is assigned to a $\sigma^* \leftarrow n$ transition, the molecules undergo direct dissociation of the C−X (X = Cl, Br, I) bond and produce alkyl radicals and halogen atoms in the ground state X ($^2P_{3/2}$) or the excited state X ($^2P_{1/2}$).[13−15] Because the fragments separate so fast, the properties related to the transition are preserved, and the observed properties of the products (i.e., the vector quantities, internal energy distributions, and branching ratio of various product states) reflect the related potential energy surface. Three repulsive electronic excited states have been assigned by Mulliken to contribute to the A-band absorption of alkyl halides, which have been identified as $^3Q_1$ (2E), $^3Q_0$ ($2A_1$), and $^1Q_1$ (3E).[16−18] Of the three states, only the $^3Q_0$ state is correlated with the spin−orbit excited state X ($^2P_{1/2}$) and the corresponding transition dipole moment is aligned parallel to the C−X bond, whereas the $^3Q_1$ and $^1Q_1$ states are correlated with the spin−orbit ground state X ($^2P_{3/2}$), and the corresponding transitions are polarized perpendicular to the bond axis.

In recent years, the ion velocity imaging technique[19] coupled with a resonance-enhanced multiphoton ionization (REMPI) scheme has been used widely to study the photodissociation of alkyl halides.[2−8] Compared to the photodissociation dynamics of alkyl halides, those of alkyl dihalides have received less attention, mainly because the dissociation pathways become more complicated. In addition to the selection of breaking a specific chemical bond, three-body photodissociation may take place in a one-photon absorption process. A well-known example is the photoexcitation of CF_2I_2 performed by Huber and co-workers.[9−12] In the present experiment, the photodissociation dynamics of $C_3H_6Br_2$ has been investigated at 234 nm using a 2D photofragment ion velocity imaging technique coupled with a [2 + 1] resonance-enhanced multiphoton ionization (REMPI) scheme. With this technique, we have obtained the spatial distributions, speed distributions, relative quantum yields, and translational anisotropies of Br* and Br fragments generated after the photolysis of $C_3H_6Br_2$.

2. Experimental Section

The experimental setup has been described in detail elsewhere.[20] In brief, the ion velocity imaging apparatus consists of a molecular beam source chamber and a main chamber that are both pumped with separate mechanical pumps and turbo pumps. The main chamber is composed of an electrostatic lens, a time-of-flight (TOF) tube, and a 2D position-sensitive detection system. A pulsed valve with a 0.6-mm-diameter orifice operates synchronously with the laser pulses, typically at 10 Hz. A 1-mm-diameter conical skimmer mounted 30 mm downstream from the nozzle divides the main chamber from the source chamber. This skimmer skims the supersonic molecular beam before it enters the main chamber.

The 355 nm output of an Nd:YAG laser [YG981E10, Quantel] operating at 10 Hz is used to pump a dye laser [ScanMate 2E OG, Lambda Physik], and the output of the dye laser is frequency doubled by a BBO crystal. The linearly polarized UV laser beam is vertically aligned using a Soleil−Babinet compensator and then focused onto the leading edge of the molecular beam by a lens with a focal length of 200 mm to minimize the effect of cluster formation. The $C_3H_6Br_2$ molecules are photolyzed by the UV laser light, and the nascent bromine atom fragments are then selectively ionized using the [2 + 1] REMPI technique within the same laser pulse. The expanded bromine ion cloud is projected onto a 2D position-sensitive detector plate that consists of a microchannel plate (MCP)/phosphor screen and a charge-coupled device (CCD) camera. A positive high-voltage pulse with 1.0 μs duration is applied to the MCP to achieve a high gain at the mass of interest. For the REMPI detection of bromine atoms, the laser wavelengths are scanned over the Doppler profile of the Br photofragments.

The liquid sample of $C_3H_6Br_2$ (99.5% purity) seeded in helium at 1 atm is introduced into the source chamber without further purification.

* To whom correspondence should be addressed. E-mail: bzhang@wipm.ac.cn. Fax: +86-27-87199291.

10.1021/jp0537097 CCC: $30.25
Published on Web 11/18/2005

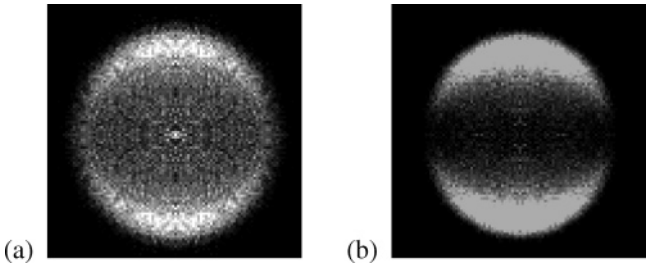

Figure 1. Raw ion images of (a) Br and (b) Br* fragments from the photolysis of $C_3H_6Br_2$ at 234 nm. In all images, the linear polarization vector of the UV laser is vertical.

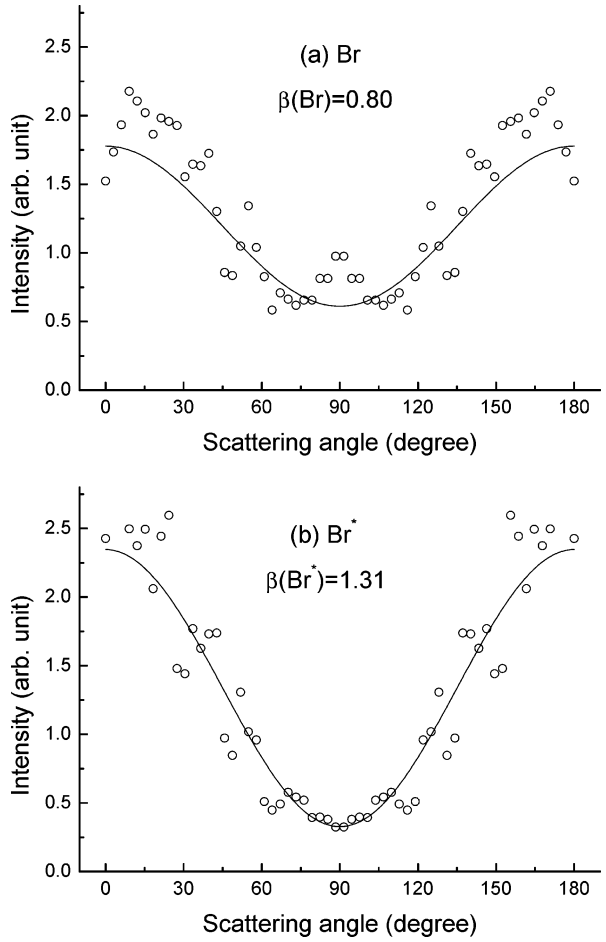

Figure 2. Angular distributions of (a) Br and (b) Br* fragments from the photolysis of $C_3H_6Br_2$ at 234 nm.

3. Results

The raw images of Br and Br* are displayed in Figure 1a and b, respectively. The polarization vectors of the laser beams are vertically aligned in both cases. Each image is accumulated over 30 000 laser shots, and the background is removed by subtracting a reference image collected at an off-resonance wavelength under the same conditions. As shown in Figure 1, the images display a polar cap appearance, implying that an electronic transition with a dipole moment parallel to the recoil axis (C−Br) provides the main contribution to the generation of bromine fragments. The more distinct structure in the image of Br* in comparison with that of Br indicates a higher anisotropy in the angular distribution of Br*.

Three-dimensional spatial (angular and speed) distributions of the fragments can be reconstructed by performing an inverse

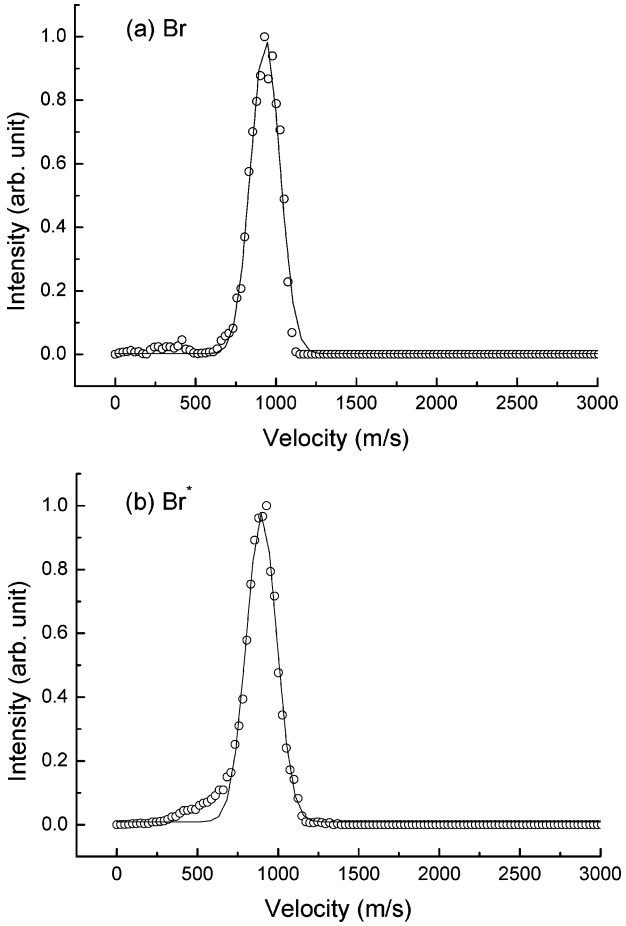

Figure 3. Speed distributions of (a) Br and (b) Br* fragments from the photolysis of $C_3H_6Br_2$ at 234 nm. The solid line indicates the curve fitted with a Gaussian function.

Abel transformation.[21] The inverse Abel transformation is very sensitive to noise, so the raw images are presmoothed using a Gaussian filter with a 7 × 7 window before performing the inverse Abel transformation to reduce the noise that may arise during the transformation. The angular distribution I(θ) can be obtained by integrating the reconstructed 3D speed distribution over a proper range of speed at each angle, and the spatial anisotropy parameter β can be extracted by fitting I(θ) into the standard formula[22,23]

$$\mathrm{I}(\theta) = (4\pi)^{-1}[1 + \beta P_2(\cos\theta)] \qquad (1)$$

where $P_2(\cos\theta)$ is the second-order Legendre polynomial and θ is the angle between the laser polarization axis and the recoil velocity of the photofragments. β(Br) = 0.80 and β(Br*) = 1.31 are extracted at 234 nm, as shown in Figure 2a and b, indicating that two or more channels are involved in the generation of bromine atoms in each state. The speed distribution $P(v)$ has been obtained by integrating the reconstructed 3D speed distribution over all angles at each speed, as shown in Figure 3. Each distribution can be well fitted by a narrow single-peaked Gaussian curve, implying that Br* and Br are generated as a result of direct dissociation via repulsive potential energy surfaces. In view of energy, one would expect the secondary dissociation of the C_3H_6Br radical to take place; however, in our experiment, we have not observed any secondary photodissociation or three-body dissociation because the speed distributions of the photofragments formed via secondary photodissociation and three-body dissociation would be broader

TABLE 1: Energy Partitioning, Anisotropy Parameters, and Velocities of Bromine Fragments for the Photodissociation of $C_3H_6Br_2$

wavelength, nm	state	intermediate state	$h\nu$, kJ/mol	$\langle E_{ava}\rangle$, kJ/mol	$\langle E_T\rangle$, kJ/mol	f_T	β	v, m/s
233.62	$Br(^2P^0_{3/2})$	$6p^4P^0_{3/2}$	512.5	215.9	57.9	0.27	0.80	934.62
233.95	$Br(^2P^0_{1/2})$	$6p^2S^0_{1/2}$	511.8	171.2	53.4	0.31	1.31	897.71

than one corresponding to the primary photodissociation channels.[1]

The available energy E_{avl} for the dissociation process is calculated by

$$E_{avl} = E_{h\nu} - D_0 - E_{el} + E_{int} \quad (2)$$

$$f_T = \frac{\langle E_T\rangle}{E_{avl}} \quad (3)$$

where $E_{h\nu}$ is the photon energy, $D_0 = 70.9$ kcal/mol[24] is the bond dissociation energy of C−Br, E_{el} is the electronic energy of the bromine atom (it is 0 kJ/mol for Br and 44 kJ/mol for Br*), E_{int} is the internal energy of the parent molecule (assumed to be zero because rotational and vibrational excitation are weak and can be negligible under the supersonic molecular beam condition), and f_T is the fraction of translational energies. The $f_T = 0.27$ for Br and 0.31 for Br* values reported in Table 1 are very close to the value of $f_T^{soft} = 0.22$, the soft radical limit of the impulsive model that accounts for the vibrational excitation. All of the dynamic properties at 234 nm photodissociation of $C_3H_6Br_2$ are listed in Table 1.

The product quantum yields of Br* and Br can be determined using the following equation[25]

$$\frac{N(Br^*)}{N(Br)} = k\frac{S(Br^*)}{S(Br)} \quad (4)$$

where $N(Br^*)$ and $N(Br)$ are the numbers of Br* and Br fragments and $S(Br^*)$ and $S(Br)$ are the measured intensities of Br^+ at the different REMPI wavelengths for the ionization of Br* and Br atoms. Factor k is determined by the REMPI probability ratios, relative detection efficiencies, and other instrumentation factors. It is obtained by performing a calibration experiment using Br_2 photolysis under the same conditions. In this work, we measured the relative quantum yield at 234 nm. The value of k was measured to be 0.349 at 234 nm. The ratio of $N(Br^*)/N(Br)$ was calculated to be 0.265 via eq 4, and the relative quantum yields of $\Phi(Br^*) = 0.21$ at 234 nm was easily obtained by the following relationships:

$$\Phi(Br^*) = \frac{N(Br^*)}{N(Br) + N(Br^*)} \quad (5)$$

$$\Phi(Br) = 1 - \Phi(Br^*) \quad (6)$$

In addition, we investigated the photodissociation of 1,3-dibromopropane in the wavelength range of 231−239 nm, and we measured $\beta(Br) = 0.78$ at 232.93 nm, $\beta(Br^*) = 1.33$ at 231.87 nm, and 1.22 at 238.57 nm. From the results, we find that the β values are quite close to the β values at 234 nm and appear to be insensitive to the photolysis wavelength.

4. Discussion

The alkyl bromides have a first absorption band that consists of three transitions from the ground state to three dissociative excited states designated as $^3Q_1$, $^3Q_0$, and $^1Q_1$ by Mulliken in descending order of energy. The $^1Q_1$ (3E) and $^3Q_1$ (2E) states are responsible for the electronic transitions that are aligned perpendicular to the C−Br bond and adiabatically correlated with the channel for Br formation, and the angular distribution $I(\theta)$ of the photofragments will follow a $\sin^2\theta$ dependence. Similarly, the $^3Q_0$ ($2A_1$) ← X transition is polarized parallel to the bond and adiabatically correlated with the Br* channel, and the angular distribution $I(\theta)$ will follow a $\cos^2\theta$ dependence. Hence, we expect $\beta(Br^*) = 2.0$ because Br* correlates to the $^3Q_0$ state and $\beta(Br) = -1$, whereas both the $^1Q_1$ and $^3Q_1$ states correlate to Br. However, as Table 1 shows, the measured $\beta = 0.80$ for Br and 1.31 for Br* are substantially different from the expected values. This suggests that a sufficient amount of the Br* produced by direct excitation is converted to Br during dissociation because of the nonadiabatic coupling between the $^3Q_0$ and $^1Q_1$ states, which adds sufficient parallel character to the otherwise perpendicular-type Br angular distribution.

TABLE 2: Contribution Ratio of the Parallel and Perpendicular Transitions

wavelength, nm	state	β	$\chi_{\parallel}$	$\chi_{\perp}$
233.62	Br	0.80	0.60	0.40
233.95	Br*	1.31	0.77	0.23

TABLE 3. Relative Fraction of Each Potential Surface at 234 nm

wavelength, nm	state	initial excitation	curve crossing
234	Br	$^1Q_1 + {}^3Q_1$ 0.316	$^3Q_0 \rightarrow {}^1Q_1$ 0.474
	Br*	$^3Q_0$ 0.162	$^1Q_1 \rightarrow {}^3Q_0$ 0.048

To estimate the relative contributions of the parallel and the perpendicular components to Br* and Br fragment formation channels, the classical relationship is used.

$$\beta = \chi_{\parallel}\beta_{\parallel} + \chi_{\perp}\beta_{\perp} \quad (7)$$

$$\chi_{\parallel} + \chi_{\perp} = 1 \quad (8)$$

where $\beta_{\parallel}$ and $\beta_{\perp}$ represent the anisotropy parameters for pure parallel and perpendicular transitions. The values of $\chi_{\parallel}$ and $\chi_{\perp}$ and the fractions for Br* and Br fragment formation channels, respectively, are listed in Table 2.

Because of the existence of a conical intersection of the $^1Q_1$ and $^3Q_0$ states, A-band excitation leads to Br production via three pathways (initial excitation to $^1Q_1$, $^3Q_1$, and a transition from $^3Q_0$ to $^1Q_1$) and Br* production via two pathways (initial excitation to $^3Q_0$ and a transition from $^1Q_1$ to $^3Q_0$). All of the possible pathways are listed in Table 3, and the relative fractions of the individual pathways have been determined from the relative quantum yield and angular distributions of bromine fragments produced in $C_3H_6Br_2$ photolysis.

The curve-crossing probability from lower PES to upper PES and that from upper PES to lower PES are denoted P_{up} and P_{down}, respectively, which can be obtained from the relationships

$$P_{up} = \frac{f(^3Q_0 \rightarrow {}^1Q_1)}{f(^3Q_0) + f(^3Q_0 \rightarrow {}^1Q_1)} \quad (9)$$

$$P_{down} = \frac{f(^1Q_1 \rightarrow {}^3Q_0)}{f(^1Q_1) + f(^1Q_1 \rightarrow {}^3Q_0)} \leq \frac{f(^1Q_1 \rightarrow {}^3Q_0)}{f(^1Q_1) + f(^3Q_1) + f(^1Q_1 \rightarrow {}^3Q_0)} \quad (10)$$

where $f(X)$ is the fraction originating from the X surface. From the above equations, we calculated $P_{up} = 0.745$ and $P_{down} \leq 0.132$ at 234 nm. The Landau−Zener model has generally been used to describe the curve-crossing phenomena in the photodissociation of alkyl halides in the A band.[4,26,27] If the Landau−Zener model is valid, then the curve-crossing probability from the $^3Q_0$ to the $^1Q_1$ surface is the same as its reverse from the $^1Q_1$ to the $^3Q_0$ surface. But the estimated probability of the curve crossing from the $^3Q_0$ to the $^1Q_1$ surface is much higher than that of the reverse, as listed in Table 3. This disagreement—the limit of the Landau−Zener model—may have resulted from the difference between the shapes of the 2D potential surface of $^3Q_0$ and $^1Q_1$. Though the Landau−Zener model holds for the diatomic molecules, it does not hold for the polyatomic molecules because of its 1D potential surface model. In recent studies, much attention has been paid to the possibility of the production of highly polarized atoms from molecular photodissociation, and strongly polarized atomic photofragments have been measured for Br.[28,29] In our work, we have neglected this possibility and will investigate it in future research.

5. Conclusions

In this work, the photodissociation dynamics of 1,3-dibromopropane has been investigated at 234 nm by means of the 2D photofragment ion velocity imaging technique. The one-photon dissociation channel is the cleavage of the C−Br bond, generating bromine atoms of ground state Br ($^2P_{3/2}$) and spin−orbit excited state Br ($^2P_{1/2}$) that are detected by [2 + 1] REMPI. We measured the recoil velocity distributions of bromine fragments, and each velocity distribution can be well fitted by a narrow single-peaked Gaussian curve, implying that Br* and Br are generated as a result of direct dissociation via repulsive potential energy surfaces. Moreover, we measured the angular distributions and the relative quantum yields of the Br* and Br fragments, and on the basis of the recoil anisotropies and relative product quantum yields, the relative contributions of the parallel and perpendicular transitions to the generation of bromine fragments have been extracted for the Br* and Br channels. The results of this work proved the existence of the curve crossing between the $^3Q_0$ and the $^1Q_1$ states, and we also investigated the relative fractions of each potential surface for bromine fragment production at 234 nm.

Acknowledgment. We gratefully acknowledge the support from the Innovation Foundation of the Chinese Academy of Sciences.

References and Notes

(1) Park, M. S.; Kim, T. K.; Lee, S. H.; Jung, K. H.; Volpp, H. R.; Wolfrum, J. *J. Phys. Chem. A* **2001**, *105*, 5606.
(2) Jung, Y. J.; Park, M. S.; Kim, Y. S.; Jung, K. H. *J. Chem. Phys.* **1999**, *111*, 4005.
(3) Kim, T. K.; Park, M. S.; Lee, K. W.; Jung, K. H. *J. Chem. Phys.* **2001**, *115*, 10745.
(4) Gougousi, T.; Samartzis, P. C.; Kitsopoulos, T. N. *J. Chem. Phys.* **1998**, *108*, 5742.
(5) Xu, H. F.; Guo, Y.; Liu, S. L.; Ma, X. X. *J. Chem. Phys.* **2002**, *117*, 5722.
(6) Lee, S. H.; Jung, K. H. *Chem. Phys. Lett.* **2001**, *350*, 306.
(7) Huang, J. H.; Xu, D. D.; Francisco, J. S.; Jackson, W. M. *J. Chem. Phys.* **2003**, *119*, 3661.
(8) Lee, S. H.; Jung, Y. J.; Jung, K. H. *Chem. Phys.* **2000**, *260*, 143.
(9) Wannenmacher, E. A. J.; Felder, P.; Huber, J. R. *J. Chem. Phys.* **1991**, *95*, 986.
(10) Baum, G.; Felder, P.; Huber, J. R. *J. Chem. Phys.* **1999**, *98*, 1999.
(11) Radloff, W.; Farmanara, P.; Stert, V.; Schreiber, E.; Huber, J. R. *Chem. Phys. Lett.* **1998**, *291*, 173.
(12) Scheld, H. A.; Furlan, A.; Huber, J. R. *Chem. Phys. Lett.* **2000**, *326*, 366.
(13) Penn, S. M.; Hayden, C. C.; Carlson Muyskens, K. J.; Crim, F. F. *J. Chem. Phys.* **1988**, *89*, 2909.
(14) Chandler, D. W.; Thoman, J. W., Jr.; Janssen, M. H. M.; Parker, D. H. *Chem. Phys. Lett.* **1989**, *156*, 151.
(15) Kim, Y. S.; Kang, W. K.; Kim, D. C.; Jung, K. H. *J. Phys. Chem. A* **1997**, *101*, 7576.
(16) Mulliken, R. S. *J. Chem. Phys.* **1940**, *8*, 382.
(17) Mulliken, R. S. *Phys. Rev.* **1942**, *61*, 277.
(18) Mulliken, R. S.; Teller, E. *Phys. Rev.* **1942**, *61*, 283.
(19) Eppink, A. T. J. B.; Parker, D. H. *Rev. Sci. Instrum.* **1997**, *68*, 3477.
(20) Tang, Y.; Ji, L.; Zhu, R.; Wei, Z.; Zhang, B. *ChemPhysChem* **2005**, *6*, 2137.
(21) Heck, A. J. R.; Chandler, D. W. *Annu. Rev. Phys. Chem.* **1995**, *46*, 335.
(22) Zare, R. N.; Herschbach, D. R. *Proc. IEEE* **1963**, *51*, 173.
(23) Zare, R. N. *Mol. Photochem.* **1972**, *4*, 1.
(24) Wentworth, W. E.; George, R.; Keith, H. *J. Chem. Phys.* **1969**, *51*, 1791.
(25) Jee, Y. J.; Jung, Y. J.; Jung, K. H. *J. Chem. Phys.* **2001**, *115*, 9739.
(26) Kang, W. K.; Jung, K. W.; Kim, D. C.; Jung, K. H. *J. Chem. Phys.* **1996**, *104*, 5815.
(27) Park, M. S.; Lee, K. W.; Jung, K. H. *J. Chem. Phys.* **2001**, *114*, 10368.
(28) Rakitzis, T. P.; Samartizis, P. C.; Kitsopoulos, T. N. *Phys. Rev. Lett.* **2001**, *87*, 123001.
(29) Rakitzis, T. P.; Samartzis, P. C.; Toomes, R. L.; Kitsopoulos, T. N. *J. Chem. Phys.* **2004**, *121*, 7222.